Remote Sensing of Environment 257 (2021) 112347

Contents lists available at ScienceDirect

Remote Sensing of Environment

journal homepage: www.elsevier.com/locate/rse

A quasi-physical sea surface temperature method for the split-window data from the Second-generation Global Imager (SGLI) onboard the Global Change Observation Mission-Climate (GCOM-C) satellite

Yukio Kurihara *, Hiroshi Murakami, Kazunori Ogata, Misako Kachi

Earth Observation Research Center (EORC), Japan Aerospace Exploration Agency (JAXA), 2-1-1 Sengen, Tsukuba-shi, Ibaraki 305-8505, Japan

ARTICLE INFO

Editor: M Wang

Keywords:
SST
Q-method
SGLI
GCOM-C
AHI
Himawari

ABSTRACT

This paper describes a quasi-physical method (the Q-method) for determining the sea surface temperatures (SSTs). The Q-method is a coefficient-based technique developed for processing the multiband infrared (IR) data of the geostationary Himawari-8 satellite. We applied the Q-method to the split-window data from the Second-generation Global Imager (SGLI) onboard the Global Change Observation Mission-Climate (GCOM-C) satellite. A comparison of the determined SGLI SSTs and buoy data shows a bias with a robust standard deviation of −0.097 K and 0.28 K in the daytime and −0.18 K and 0.28 K at night, respectively. Meanwhile, high biases of nearly −0.5 K were calculated for SSTs at and around 305 K. A residuals analysis suggests that the high negative bias is caused by insufficient information on the atmospheric correction brought by split-window data. This paper discusses the physical and mathematical background of the Q-method and compares it with another coefficient-based physical scheme.

1. Introduction

Satellite-based remote sensors are expedient in the monitoring of the sea surface temperatures (SSTs) because they can observe the Earth with high resolution and at frequent intervals. Satellite-based SSTs have decades of history (e.g. O'Carroll et al., 2019; Minnett et al., 2019) and have generated several important data sets (e.g. Merchant et al., 2019; Casey et al., 2010; Kilpatrick et al., 2015; Ignatov et al., 2016).

The determination of SSTs from thermal infrared (IR) images dates back to the 1970s (Anding and Kauth, 1970; Prabhakara et al., 1974; McMillin, 1975), when SSTs were estimated by correcting the brightness temperatures (BTs) for atmospheric attenuation using differences between BTs (BTDs) measured by two split-window channels or at two different viewing angles. This is known as the split-window method. The split-window method developed into the multi-channel SST (MCSST) method (McClain et al., 1985) and the nonlinear SST (NLSST) method (Walton et al., 1998), among others (e.g. Kilpatrick et al., 2001; Petrenko et al., 2014). These methods, which are calculated by regression analysis, are categorized as empirical regression methods.

Aside from empirical methods, there are physically based methods. Závody et al. (1995) developed a coefficient-based scheme for retrieving SSTs from the along-track scanning radiometer (ATSR). They generated coefficients using simulated ATSR data and instrumental noise. The ATSR data were simulated numerically using atmospheric profiles of temperature and water vapor obtained by ships and coastal stations and SSTs estimated from the surface air temperature. The coefficient-based scheme was refined by Embury et al. (2012b) using the total column of water vapor provided by numerical weather prediction (NWP) analyses (Embury et al., 2012b; Embury and Merchant, 2012; Embury et al., 2012a). Nalli and Smith (1998) proposed the physical multi-window SST (PWSST) method. PWSST uses the deviation technique (Smith et al., 1991), an application of differential calculus, to solve the radiative transfer equation. Merchant et al. (2008) and Koner et al. (2015) applied optimal estimation (OE) and modified total least squares (MTLS) methods to determine SSTs.

The quasi-physical SST method (Q-method) was developed to determine SST (QSST) using the multiband IR data from the Advanced Himawari Imager (AHI) onboard the Japanese Himawari-8/9 satellite (Kurihara et al., 2016). The Q-method is a physically based regression method that determines the skin SST as an approximate solution to the radiative transfer equation. Coefficients are generated using a radiative transfer model (RTM) and NWP data in advance. It is important to select the NWP data for a period that does not overlap that of satellite data. It improves the independence between retrieved SSTs and NWP. The Q-

* Corresponding author.
E-mail address: kurihara.yukio@jaxa.jp (Y. Kurihara).

https://doi.org/10.1016/j.rse.2021.112347
Received 12 June 2020; Received in revised form 31 January 2021; Accepted 8 February 2021
Available online 19 February 2021

method excludes bias correction and all other empirical adjustments. Yang et al. (2020) compared Himawari-8 QSSTs with the skin SSTs measured with the infrared SST autonomous radiometer (ISAR) (Donlon et al., 2008) installed on the research vessel (RV) Investigator of the Australia Commonwealth Scientific and Industrial Research Organisation (CSIRO) (Beggs et al., 2017). They report bias and standard deviation of 0.09 K and 0.30 K for the Himawari-8 QSST.

The Second-generation Global Imager (SGLI) is the optical sensor onboard the Global Change Observation Mission-Climate (GCOM-C) satellite. GCOM-C is a sun-synchronous polar-orbiting satellite launched by the Japan Aerospace Exploration Agency (JAXA) in December 2017 (Imaoka et al., 2010). SGLI has spatial resolutions that can be switched between 205×250 m and 1×1 km and obtains global data via the scans for two or three days (Appendix A). SST is determined from the data obtained from the SGLI split-window channels at 10.8 and 12.0 μm. We modified the original Q-method to apply it to the split-window data.

This paper discusses the modified Q-method and its validation result. The discussion refers to the modified Q-method as the Q-method as long as there is no risk of confusion, and SST denotes the skin SST unless otherwise noted. Section 2 introduces the Q-method, Sections 3 and 4 discuss the physical background and performance of the Q-method, and validation results for retrieved SSTs are discussed in Sections 5 and 6. Section 7 concludes with a summary. GCOM-C and SGLI are outlined in Appendix A. A sensor-specific conversion from the radiance to SST is described in Appendix B. The mathematical background of the Q-method is discussed in Appendix C. Appendix D summarizes the notation used in the discussion.

2. The SST method

An SST (T_s) is derived from the radiance (I_s), which in turn is determined by

$$I_s = I_{s0} + \mathbf{a}^T(\mathbf{I} - \mathbf{I}_0) \tag{1}$$

Here, $\mathbf{a}$ and $\mathbf{I}$ are the column vectors of coefficients and IR data, respectively. The T on the shoulder of $\mathbf{a}$ denotes the transpose of the vector. I_{s0} and $\mathbf{I}_0$ denote pre-calculated initial data. I_s and I_{s0} are the radiances of blackbodies which have the surface temperatures of T_s and T_{s0}. The wavelength is omitted to simplify the formula. Note that IR data is the same as the radiance at the top of the atmosphere (TOA). Eq. (1) is equivalent to the first-order Taylor polynomial at $\mathbf{I} = \mathbf{I}_0$.

Initial data, I_{s_0} and $\mathbf{I}_0$ will be referred to as the anchor point. Deviation from the anchor point will be denoted by Δ, such that $\Delta\mathbf{I} = \mathbf{I} - \mathbf{I}_0$. The conversion from I_s to T_s is made by combining a regression formula and the inverse of the Planck function. The regression formula is introduced to take the sensor characteristics into account. Details on the conversion are discussed in Appendix B.

The Q-method uses a look-up table for initial anchor points and coefficients, which are generated for bins for the chosen SZAs (Fig. 1) in advance. In determining SST, an anchor point and coefficients are generated from the initial anchor points and coefficients by linear interpolation at the SZA of the satellite data. We chose BT and BTD as the keys to the initial anchor points because BT is easier to handle than the radiance.

3. Physical background

3.1. Assumptions

The Q-method was initially developed for real-time retrieval. Since the accuracy of real-time external data was unknown, assumptions were made that would avoid the use of such data. However, some high-accuracy external data could be available with reprocessing. Furthermore, it is also possible that external data improve SSTs retrieved in real-time. Thus, it is important to expand the Q-method to handle these external data. Expansion of the Q-method is left for the future.

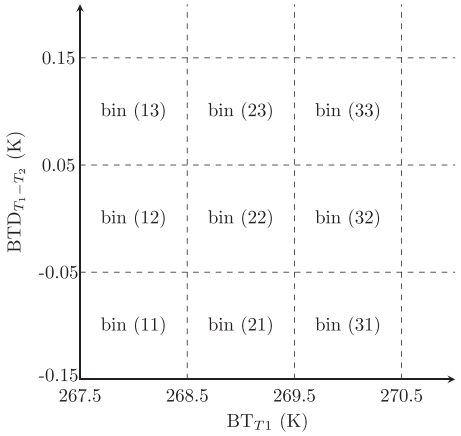

Fig. 1. Bins on the BT-BTD plane. BT$_{T_1}$ denotes the brightness temperature at the T1 channel, and BTD$_{T_1-T_2}$ denotes the brightness temperature difference determined by BT$_{T_1}$−BT$_{T_2}$. Each bin size is 1 K × 0.1 K.

3.1.1. Clear sky

We derived the Q-method from the radiative transfer equation for the clear sky, which is a common requirement for detecting IR SSTs. Cloud contamination can result in damage to retrieved SSTs that makes it difficult to evaluate SST methods. Referring to previous researches (e.g. Merchant et al., 2008), this paper uses robust statistics (the median and the robust standard deviation (RSTD) (e.g. Huber and Ronchetti, 2009, p. 106)) for validating the SGLI QSST. Although cloud contamination is a central issue, it is beyond the scope of this research.

3.1.2. Aerosols

Aerosols, including dust and volcanic ash, seriously impacts SST determination. Not only do absorb IR radiation, but they also change the ratio of the optical depth of the atmosphere (known as the β ratio) (Pavolonis, 2010; Závody et al., 1995; Inoue, 1987) and impairs atmospheric correction. Despite this, we did not take aerosols into account because there is no accurate real-time information about them available. However, degradation by aerosols, such as Mt. Pinatubo ash (e.g. Reynolds, 1993) and Saharan dust (e.g. Foltz and McPhaden, 2008), must be corrected for to generate accurate climatological SSTs. Aerosol correction is an issue with the Q-method that we have left to future investigation.

3.1.3. Sea surface emissivity

Sea surface emissivity varies with the emission angle and surface roughness. Previous research has proposed models that determine sea surface emissivity at a given emission angle and surface wind speed (e.g. Masuda et al., 1988; Watts et al., 1996). However, it is unknown if the wind data available in real-time is sufficient to improve the accuracy of determined SSTs. Hence, we assumed that the wind speed is constant. As the result, the sea surface emissivity depends on only the satellite zenith angle (SZA). Here, SZA and the emission angle are the same in satellite-based remote sensing. Emissivities are determined in RTM at the empirically chosen constant surface wind speed of 5 m/s for each SZA.

3.2. Formulation

Most of the regression-based SST methods are developed from the well-known split-window method, which is based on an approximation formula:

$$T_s \simeq T_1 + \eta(T_1 - T_2) \tag{2}$$

where T_1 and T_2 denote BTs of the split-window and η is a coefficient

derived from first-order approximations of the atmospheric transmittance (e.g. Liou, 2002, p. 385–387). Eq. (2) is derived by combining the radiative transfer equations for the split-window channels:

$$I = I_s t + (1-t)\bar{I}_{\uparrow}, \tag{3}$$

where t and $\bar{I}_{\uparrow}$ are the atmospheric transmittance and the mean atmospheric up-welling emission, respectively.

A serious problem with the split-window method is that biases are generated at SZAs larger than ~40° (McClain et al., 1983). This is likely to be caused by the split-window method, which does not consider the variation of the emission angle and the geometric radiation path length. To fix this problem, empirical regression-based methods typified by MCSST have added correction terms that include SZA (e.g., *sec*(SZA) − 1). Other problems may be caused by the translation from (3) to (2). The translation requires an approximation of the Planck function with a first-order polynomial. For example, the first-order polynomial calculated for BTs from 265 to 300 K generates systematic errors from −0.68 to 1.2 K on BT at 10.8 μm and those from −0.078 to 0.14 K on BTD (10.8μm − 12.0μm). Note that these errors are implicit in (2). BT and BTD are independent and closely involved in the first-order approximation of SST and the atmospheric correction, respectively. It can be inferred that those errors generate complicated noise in retrieved SST data. Furthermore, this complexity may be increased by the insensitivity of the split-window data to WV (Subsection 6.1).

These problems are caused by the first-order approximation of radiative transfer, so they can be improved by narrowing the range of parameters. The basic idea of the Q-method is to solve the radiative transfer equation in a small space. We addressed these problems by using coefficients generated at almost evenly distributed anchor points and by solving the radiative transfer equation in the neighborhood of each anchor point. To avoid the errors caused by approximating the Planck function, calculations were made on a radiance base. We regarded the radiative transfer as a projection onto a three-dimensional space defined by BT, BTD, and SZA. Eq. (1) is derived by solving the first-order Taylor polynomials of the radiative transfer equation at each anchor point. The mathematical background of the Q-method is discussed in Appendix C in detail. Note that it is possible to generate coefficients for other variables related to the IR radiative transfer as well as those for SST and that the generated coefficients determine a pseudo-inverse model of the radiative transfer defined by a pseudo-inverse matrix (Appendix C).

4. Performance

4.1. Determination accuracy

The performance of the Q-method was evaluated with over three million SGLI data points numerically generated by applying the Radiative Transfer for TOVS (RTTOV) 10.2 on NWP data. RTTOV was developed at the Numerical Weather Prediction Satellite Application Facility (NWP SAF) of the European Organisation for the Exploitation of Meteorological Satellites (EUMETSAT) (Saunders et al., 2012). The NWP data consisted of atmospheric temperature and water vapor fields objectively analyzed for the 15th of each month of 2013 provided by the Japan Meteorological Agency (JMA). The initial anchor points and coefficients were generated at SZAs of 0, 10,…, 50, 52,…, and 60° using the NWP data objectively analyzed for the 1st, 11th, and 21st of each month of 2013. We did not take NEΔT into account. Results are shown in Figs. 2 and 3. Bias and STD of all the data are 0.035 K and 0.35 K, respectively. A high negative bias of almost −1 K was calculated at SSTs ~305 K (Fig. 2).

4.2. Sensitivity and robustness

We evaluated the Q-method's sensitivity to SST variation and robustness against variations in the atmospheric water vapor (WV)

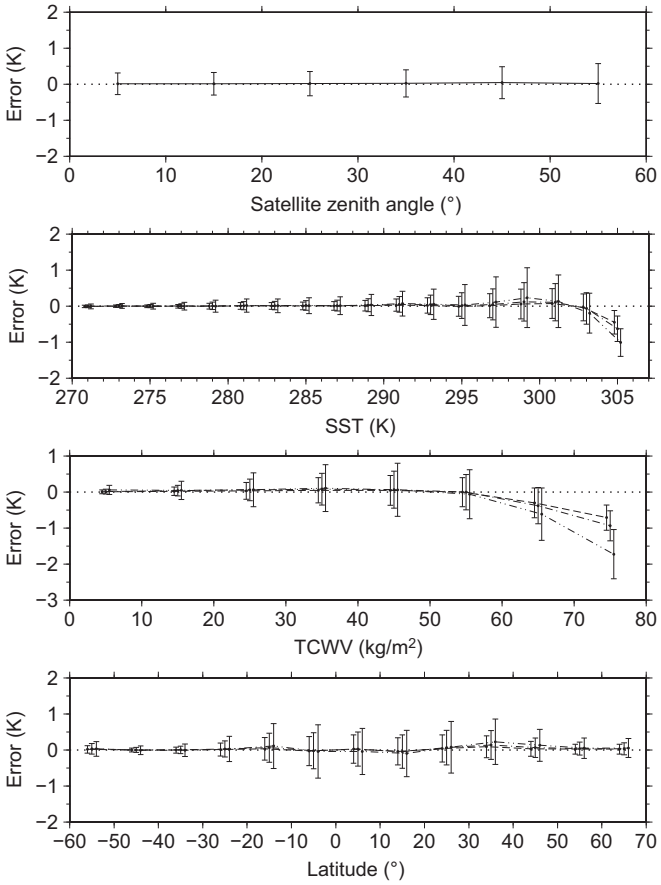

Fig. 2. Application of the Q-method to SGLI. TCWV is the Total Column Water Vapor. Dashed, single-dotted, and double-dotted lines refer to the mean errors at SZAs of 5°, 35°, and 55°, respectively. Error bars show the STD of the error.

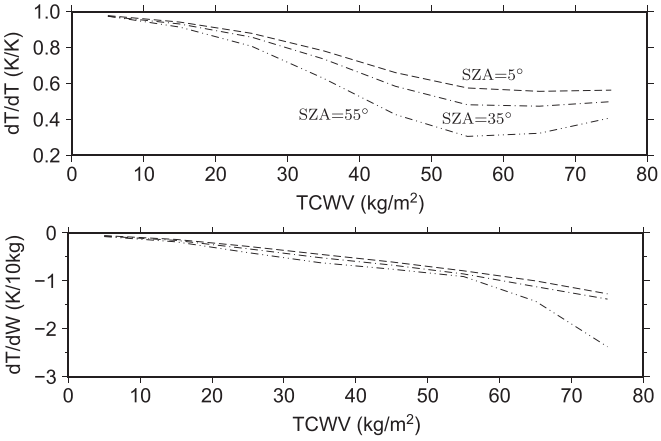

Fig. 3. Sensitivity of Q-method for SGLI.

according to Merchant et al. (2009a). Not only Accuracy, sensitivity, and robustness are all important in determining satellite-detected SSTs. We estimated the sensitivity by $<(T_{ret} - T_{ret}')/(T - T')>$. Here, T_{ret} and T_{ret}' denote retrieved SSTs, and T and T' are the true SSTs. Angle brackets denote an ensemble average. Sensitivity is a dimensionless quantity associated with the accuracy of differences in determined SSTs between two points or two different observation times (or spatial/temporal gradients of determined SSTs). If the SST method is insensitive to SST variation (i.e. sensitivity is less than 1), SST gradients would be undervalued and result in blurred SST fronts and other faults. Robustness

against WV variation was estimated by $<(T_{ret} - T_{ret}')/(W - W')>$ where W and W' denote TCWV. We calculated robustness as an average of changes in SST generated by a change in TCWV of 10 kg/m^2. TCWV can vary around fronts and coastal seas because of the exchange of the atmosphere between land and ocean. If the variation in affected SST determination (i.e. the robustness) is not zero, the accuracy of retrieved SSTs would suffer.

Sensitivity and robustness were assessed using SGLI simulation data. Sensitivity was evaluated using the T' generated by adding random variations (ΔT) less than 5 K: $T' = T + \Delta T$. The T_{ret}' was determined from SGLI data simulated by using the T' and WV; here, no change was applied to the WV. Robustness was evaluated using the W' generated by adding random variations less than 10% of the W: $W' = W + \Delta W$ where $\Delta W/W < 0.1$. Procedures for the evaluation were the same as those for evaluating the sensitivity. The result suggests a strong influence of WV over the SST determination (Fig. 2). The figure shows that sensitivity and robustness deteriorated significantly at high TCWV. Meanwhile, sensitivity is found to have improved at SZA of 55° and TCWV above 60 kg/m^2 (see the top of Fig. 2). This could be caused by degradation of the sensitivity test, numerical problems with the coefficients of the Q-method, or errors in the simulated SGLI data. The influence of high WV will be discussed in Subsection 6.1.

4.3. Impact of surface wind speed

The Q-method is premised on the sea surface emissivity estimated with a constant surface wind speed (Subsection 3.1) but, in reality, the wind speed is variable so the emissivity also varies with it. Discrepancies between the actual wind speeds and the assumed constant wind speed will generate biases in the determined SSTs. To evaluate the bias caused by an unexpected wind speed, we simulated SGLI data at each surface wind speed between 0 and 60 m/s and determined QSSTs from the generated data. Fig. 4 shows the biases calculated for each SZA. As the figure shows, the biases are less than 0.05 K at the SZAs of 5° and 35°. However, the biases are slightly higher for an SZA of 45°, and those were around 0.2 K for winds of 50 m/s or higher and at an SZA of 55°.

5. SGLI SST

We retrieved QSSTs from the SGLI data from January to March of 2019 and compared the result with buoy data. QSSTs were determined by using the same initial anchor points and coefficients as those generated for the performance evaluation (Section 4). We also determined another set of SGLI SSTs using a coefficient-based scheme and compared the result with the QSSTs.

5.1. Coefficient-based scheme (N2SST)

Our coefficient-based scheme followed Embury and Merchant (2012). We will refer to the SGLI SSTs determined by this scheme as N2SST which denotes nadir-view two-channel SSTs. N2SST is determined with a formula:

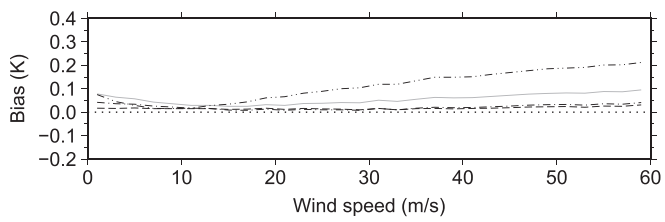

Fig. 4. Bias caused by the surface wind speed. Dashed, single-dotted, and double-dotted lines refer to the biases at SZAs of 5°, 35°, and 55°, and the solid gray line refer to those at an SZA of 45°.

$$T_s = a_0 + \mathbf{a}^T\mathbf{T} \quad (4)$$

where $\mathbf{a}$ and $\mathbf{T}$ are the column vectors of coefficients and brightness temperatures, respectively, and the a_0 is the offset. Coefficients were generated for tropical, mid-latitude, and high-latitude regions (Table 1) according to Závody et al. (1995). Each regional coefficient was calculated at each SZA using the same numerical data used to generate the initial anchor points and coefficients of QSST. SZAs are also the same as those of the initial anchor points. Note that the assumption about the sea surface emissivity also underlies N2SST.

5.2. SGLI data

We used SGLI data at the 1-km spatial resolution. The SGLI data points suspected to be cloudy were excluded based on a combination of a threshold-based test and Bayesian inference. In the threshold-based test, the STD of the horizontal QSST gradient was calculated with the data over a 3×3-pixel template then evaluated with a threshold of 0.6 K/km. This threshold is about twice as large as the random noise estimated in QSST. Cloud probability was calculated with the data: VN8 and SW2 (Table A.5) for daytime and T1, T2, and objectively analyzed daily SSTs for nighttime. The daily SSTs were provided by JMA. The probability density function (PDF) was generated by using the SGLI data and the retrieved QSSTs for March to August 2018. The threshold of 0.2 was chosen empirically as the lowest cloud probability. Note that the threshold is not fully accepted because it depends on the sensitivity to clouds and accuracy of the data. SSTs that have passed the cloud test will fall into the best SST provided in the JAXA product.

5.3. In-situ data

Because QSST is determined as a skin SST, retrieved QSSTs ought to be validated using in-situ skin SST data (e.g. Minnett et al., 2001; Donlon et al., 2008). However, there are considerably fewer in-situ skin SST data available than buoy data, so the total volume of data is not sufficient to assess the accuracy of QSST adequately. Hence, we followed the traditional method of validating satellite SSTs. Drifting- and moored-buoy

Table 1
Geographical region for N2SST.

Region	Latitude (deg)	SST (K)			
		Mean	STD	Low	High
Tropic	−25-25	301.3	1.84	286.9	305.4
Midlatitude	−50 to −25, 25-50	289.7	6.16	272.2	304.6
High-latitude	−82 to −50, 50-82	277.9	3.3	271.2	293.6

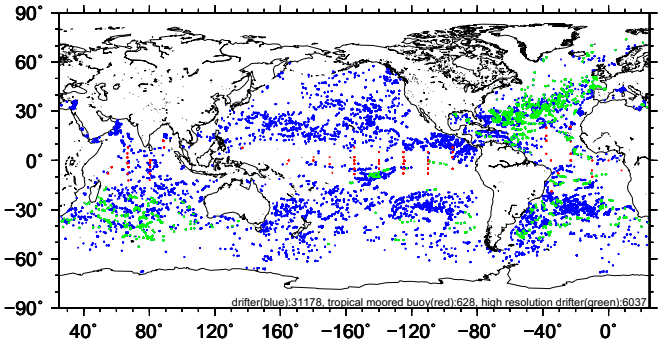

Fig. 5. Locations of buoy data in the daytime. Red, blue, and green denote the locations of moored (total number is 628), drifting (31,178), and high-resolution drifting buoys (6037), respectively. (For interpretation of the references to colour in this figure legend, the reader is referred to the web version of this article.)

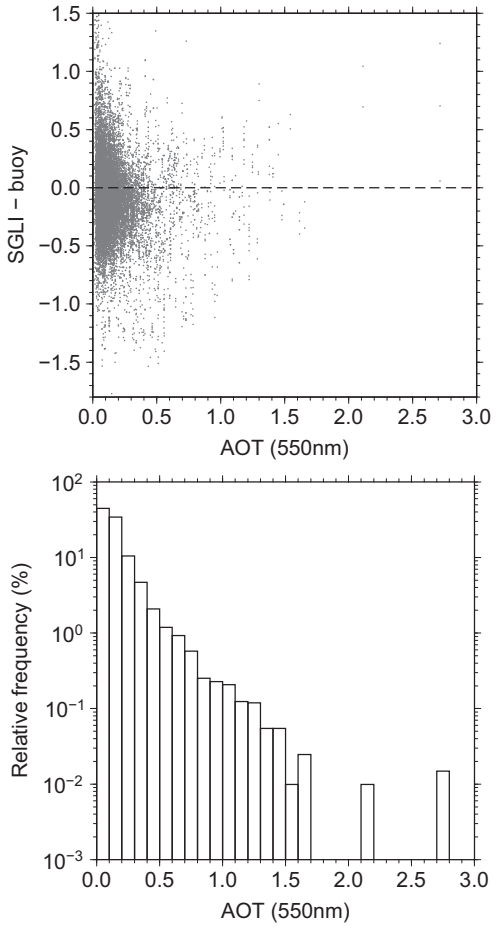

Fig. 6. Aerosol optical thickness (AOT) and deviation of QSST. The figure at the top shows deviations of the QSST from buoy data as a function of the aerosol optical thickness (AOT) at 550 nm. The figure at the bottom shows the relative frequency of AOT. The AOTs were retrieved as well as QSST using VNR data of SGLI.

data were downloaded from the In-situ SST Quality Monitor (*i*Quam) version 2.10 of the National Oceanic and Atmospheric Administration (NOAA). We used the buoy data that passed all of quality control (QC) checks of the *i*Quam (Xu and Ignatov, 2014). Each buoy data point was associated with the nearest SGLI SST in the 3 km × 3 h matchup window centered on the buoy. The total number of daytime matchups was 37,843; of nighttime, 33,004 (Fig. 5).

5.4. Impact of aerosol

Fig. 6 shows the relation between the aerosol optical thickness (AOT) and discrepancies between QSST and buoy data for the daytime. AOTs were retrieved from the VNR data of SGLI (Yoshida et al., 2020). Although the deviations tend to become negative as AOT increases, there is no clear correlation, suggesting that the influence of aerosols was not serious in the validation.

5.5. Result

Table 2 and Figs. 7-9 show the results of the comparison. Biases are almost constant at over all the SZAs for both Q- and N2SSTs (Fig. 7). If the assumption on sea surface emissivity is not suitable, biases that vary with SZA will result. Therefore, these results suggest the assumption on the sea surface emissivity is adequate to determining SSTs at SZAs $\leq 50^{\circ}$. Also, Fig. 8 shows high negative biases that were calculated in QSST around 305 K, but they did not appear in N2SST. High negative biases

Table 2
Statistics for January to March 2019.

	Bias						
	Mean	Median	STD	RSTD	Outlier	N	Clear-%
	Daytime						
QSST	−0.086	−0.097	0.36	0.28	0	37,843	10.4
N2SST	−0.13	−0.14	0.36	0.29	0		
	Nighttime						
QSST	−0.23	−0.18	0.58	0.28	133	33,004	7.7
N2SST	−0.29	−0.23	0.61	0.30	170		

Mean: mean bias, STD:standard deviation, RSTD: robust standard deviation, Outlier: the total number of the data where |SGLI−buoy| > 4., and N: the total number of the data.

will be discussed in Subsection 6.1. The difference between N2SST and QSST will be discussed in Subsection 6.2. Except for these negative biases, all biases in QSSTs were within acceptable limits considering the cool-skin or the warm-layer effect (e.g. Fairall et al., 1996; Donlon et al., 1999; Gentemann et al., 2003). Bias and STD are relatively high and large at night; this is likely to originate from the difficulties resulting from cloud masking at that time.

6. Discussion

6.1. Negative bias

As discussed in Section 5, a high negative bias was calculated for QSSTs determined for buoy data of ~305 K. On the other hand, the result of the performance evaluation suggests that QSSTs determined for SSTs of ~302 K or higher have high negative biases (the second chart in Fig. 2). The result also suggests that high negative biases are generated where TCWV >60 kg/m^2 (the third chart in Fig. 2). In general, the amounts of WV will be higher for higher SSTs, so, it can be inferred that negative biases are related to WV in the atmosphere.

We analyzed residuals for the Q-method to clarify the relation between negative bias and TCWV. Fig. 10 shows the residuals in the neighborhood of (T1, T1-T2) = (286.6 K, 3.94 K) at 60˚ of SZA, where SST takes values between 297 K and 304 K and TCWV between 40 kg/m^2 and 70 kg/m^2. There is no correlation between the residuals and the split-window data (Fig. 10 A-C), suggesting that SSTs cannot be improved any further with only the given satellite data. This suggests that errors in QSSTs are generated by the limited satellite information rather than by issues with the Q-method.

Meanwhile, a nearly linear correlation is found between the residuals for SSTs and those for the optical thicknesses of the atmosphere (Fig. 10 D). Note that the optical thickness is determined as well by the Q-method (Appendix C). The optical thickness is a physical quantity connected with the atmospheric attenuation and should be removed by the SST method. The optical thickness of IR is dominated mostly by WV (e.g. Roberts et al., 1976). Therefore, the correlation in Fig. 10 D suggests a relation between WV and the errors in determined SSTs. Considering all discussions on Fig. 10 has led the researchers to infer that discrepancies between determined SSTs and their true values originate from the limited information about WV that can be determined from split-window data. Fig. 10 suggests also that the limited information increases the uncertainty of determined SSTs. Note that the sensitivity and robustness are also degraded by the limited WV information.

Fig. 10 D says that the average error is negative where TCWVs are above the average and it is positive if TCWVs are below the average. The average of all errors in Fig. 10 is nearly zero because WV-dependent errors tend to offset each other. This argument holds for all bins in Fig. 1. As a result, SSTs are expected to have almost no bias if we see bias as a function of BT, BTD, or SAZ. However, it would not hold if we consider bias as a function of TCWV. Negative biases would predominate near the upper limit of TCWV because of the absence of positive bias to

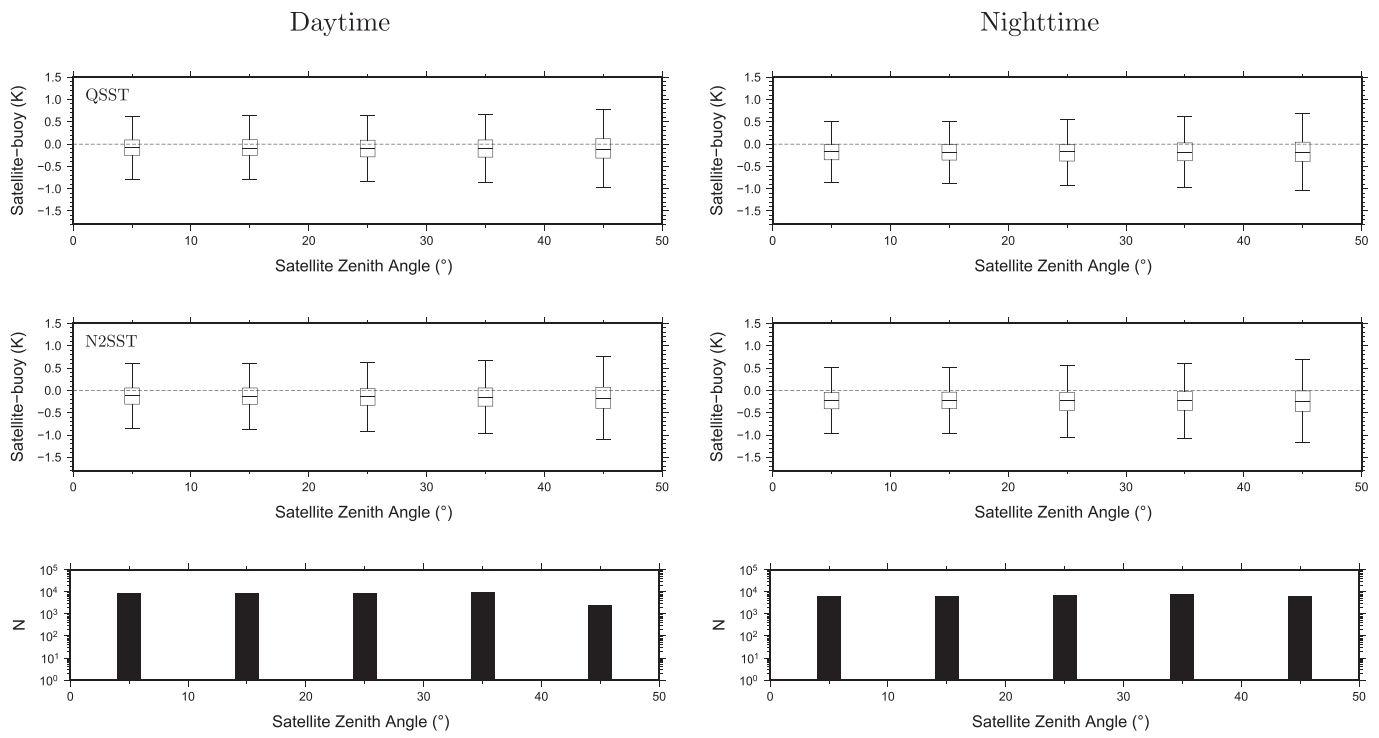

Fig. 7. SGLI SST vs. buoy data. The horizontal line in each box indicates the second quartile (the median), and the upper and lower boundaries of the box denote the first and third quartiles. The ends of the range line show the highest and lowest data within a 1.5×interquartile range (IQR): the first quartile subtracted from the third quartile. The bottom column charts denote the number of data points.

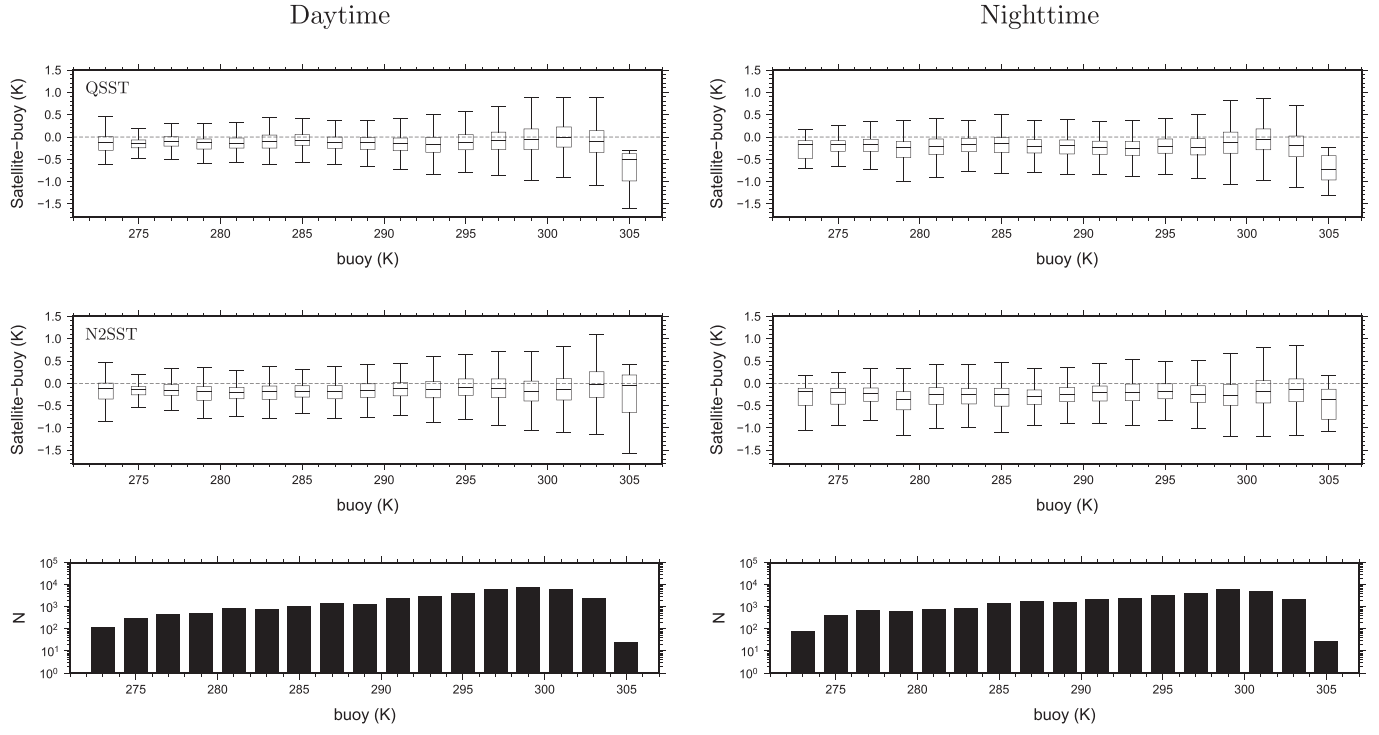

Fig. 8. SGLI SST vs. buoy data (2).

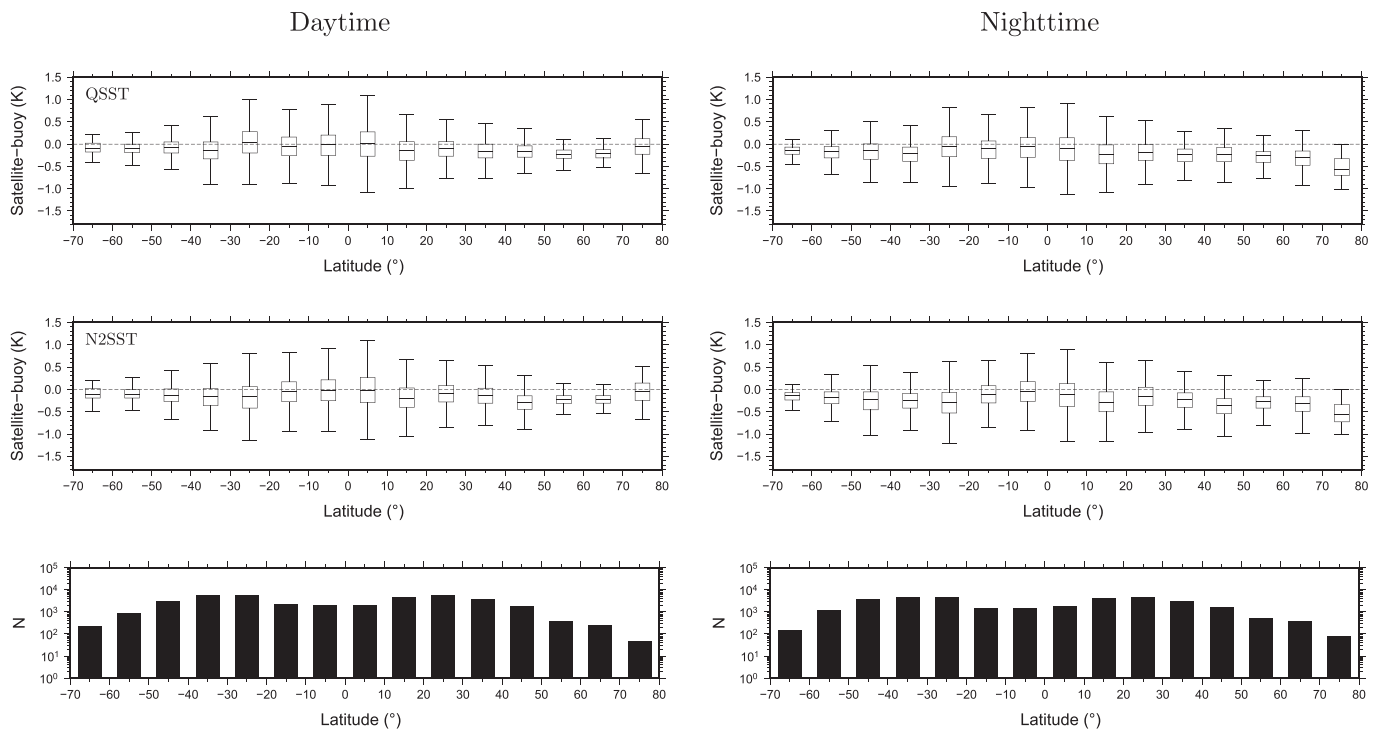

Fig. 9. SGLI SST vs. buoy data (3).

offset the negative bias.

We see that high negative biases at ~305 K are generated by the combination of high amounts of WV and limited information provided by the split-window data. According to Fig. 2, a high negative bias can predominate where the TCWV is ~60 kg/m^2 or higher. On the other hand, positive biases were not conspicuous where the WV is below the average. This may be caused by better atmospheric corrections at smaller WVs. Note that this argument cannot be applied to bias in small regions, because offsets of WV-associated biases do not necessarily occur in a small region, resulting a regional bias.

Fig. 11 shows the frequency of appearance of TCWV that was calculated by using NWP data. The figure shows that the relative frequency of TCWV, which exceeds 60 kg/m^2, is ~2% of the total and that more than 98% of them are calculated between 30 ˚S and 30 ˚N of latitudes. Fig. 12 shows the frequency of appearance of the TCWV exceeding 60 kg/m^2 at each SST range. Figures suggest that TCWV exceeds 60 kg/m^2 at a probability from 5 to 20% at SST above 302 K. Hence, it is easily inferred that negative bias is not rare in SSTs in equatorial seas retrieved from the split-window data. A lower sensitivity to WV of the split-window data was reported by Merchant et al. (2009b). Furthermore, many studies have reported systematic biases of split-window SSTs of equatorial seas (e.g. Embury and Merchant, 2012). It was concluded that information provided by split-window data is not sufficient to determine SSTs of equatorial seas or those behind high WV.

6.2. QSST and N2SST

This section analyzes the results of comparing QSST and N2SST as presented in Section 5.

Table 3 shows major differences between the Q-method and the scheme for N2SST (N2). The biggest difference would be the data. N2 determines the SST from BTs, while the Q-method calculates the SST in a radiance space. As discussed in 3.2, the use of BT involves a problem arising from the approximation of the Planck function (the BT issue). Coefficients are also remarkable in the difference between the two methods. Coefficients of N2 are generated at only three latitudinal regions, meanwhile the Q-method uses coefficients generated at numerous anchor points.

The most remarkable difference would be the negative bias discussed in Subsection 6.1. Fig. 8 shows no such bias in N2SST. This is likely to result from the regional coefficients of the N2-scheme; the N2-scheme uses coefficients generated for tropical regions. Inevitably, coefficients are adjusted for high WV conditions in tropical regions. This is why we believe biases are improved at N2SSTs around 305 K. That is, the regional coefficients of N2 improve the bias originating from the insensitivity of the split-window data to WV (the WV issue). However, uncertainty caused by the WV issue is likely to remain in N2SST, as suggested by the range lines at higher SSTs (Fig. 8). Meanwhile, the Q-method does not refer to any information for WV, so the WV issue is not improved in QSSTs. Accuracies of QSST and N2SST are almost the same, even though QSSTs were determined using coefficients to a greater extent than were N2SSTs. This is likely to be caused by the WV issue with QSST. However, it should be noted that a regression model, shown by the dashed line in Fig. 10 D, is also calculated at each anchor point. Calculated regression models are expected to improve the WV issue in QSST by using external data.

The BT issue did not seriously impact N2SSTs. Except for the negative bias, no significant difference is found between temperature-dependent and latitudinal biases for N2- and QSST. Noting that the BT issue is improved by narrowing the SST range, we infer that regional coefficients ameliorated the BT issue because of the narrow SST range in each region. Meanwhile, a slightly high bias and uncertainty (Table 2) were likely caused by the BT issue. However, the differences are quite small between N2- and QSST, and it is difficult from the results to conclude that the BT issue degrades N2SST.

6.3. Numerical uncertainty vs. the RSTD

Because the Q-method has been calculated in a numerical space, it is interesting to note how well the Q-method reflects reality. We compared the theoretically estimated uncertainties with STD/RSTDs derived by comparison with buoy data. The uncertainties were estimated by taking

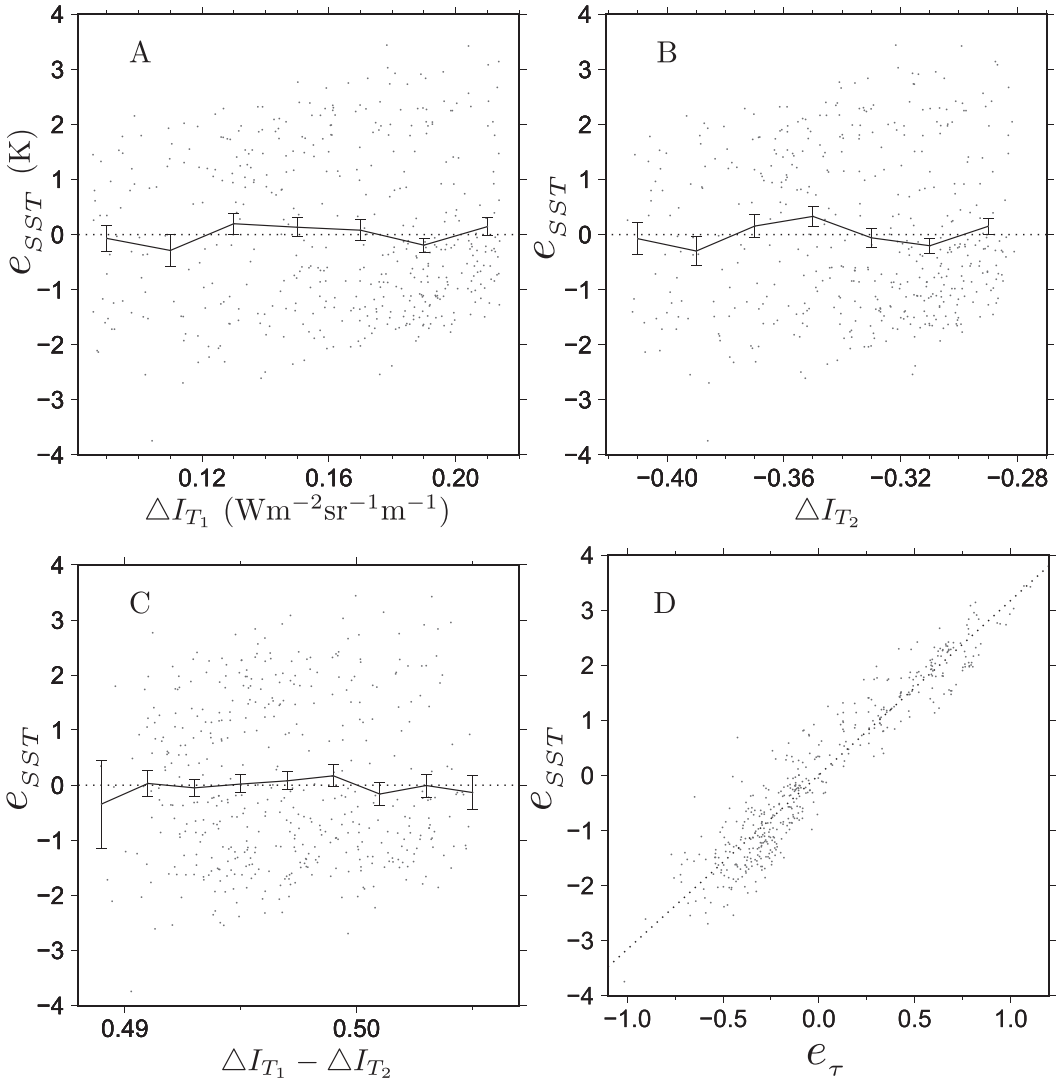

Fig. 10. Residuals for the coefficients generated in the neighborhood of (T1, T1−T2) = (286.6 K, 3.94 K) at SZA of 60°. e_{SST} and e_τ are the residuals for SST and τ, respectively. Solid lines and error bars in A-C show the mean residual and the standard error (STE) of the mean residual, respectively. STE is determined by STD divided by $\sqrt{N}$. The dotted line in D is the regression line.

NEΔT (Table A.5) into account. Fig. 13 shows the uncertainties and RSTDs for comparison. Estimated uncertainties represent RSTDs well, however, they are slightly high. Note that these overestimates apply also to STD. However, estimated uncertainties are still meaningful to NWP and other objective analyses.

We consider these overestimates can be caused by the quality control performed on NWP data. We checked NWP data for quality control by testing WV at each atmospheric layer. NWP data were excluded as cloudy if WV was saturated at least one layer. Here, we used Tetens's formula, which gives the saturation WV pressure. As a result, all of the NWP data were used to calculate the Q-method if WV was not saturated in all layers (even if it was nearly saturated in a few layers), which may increase the numerical uncertainties. The clear/cloud threshold for NWP data should be reviewed.

7. Conclusion

We applied the Q-method to the split-window data obtained with the SGLI optical sensor onboard the GCOM-C satellite. The Q-method is an integrated method of local linear models that are derived from the IR radiative transfer equation. The Q-method is supported by rigorous mathematical derivation. The physical and mathematical backgrounds of the Q-method were discussed in detail.

QSSTs retrieved by performing the Q-method on SGLI data were compared to buoy data and another set of coefficient-based SGLI SSTs (N2SSTs). The comparison shows a bias (median) and STD (RSTD) of −0.086 K (−0.097 K) and 0.36 K (0.28 K) for daytime and − 0.23 K (−0.23 K) and 0.58 K (0.28 K) for nighttime. Biases were almost constant for all SZAs. The same applies to N2SST, suggesting that a wind speed of 5 m/s is a suitable assumption for sea surface emissivity. However, an investigation result derived using numerically simulated SGLI data says that QSSTs at SZAs of 45° or above may include a bias generated by unexpected surface winds, Estimated bias values reached ~0.2 K at an SZA of 55° for wind speeds of ~50 m/s or higher.

A high negative bias was found in QSST at ~305 K. High negative biases are likely to have originated from high amounts of WV in the atmosphere. A performance evaluation suggests that negative bias will predominate if TCWV is ~60 kg/m^2 or higher. Residuals for the Q-

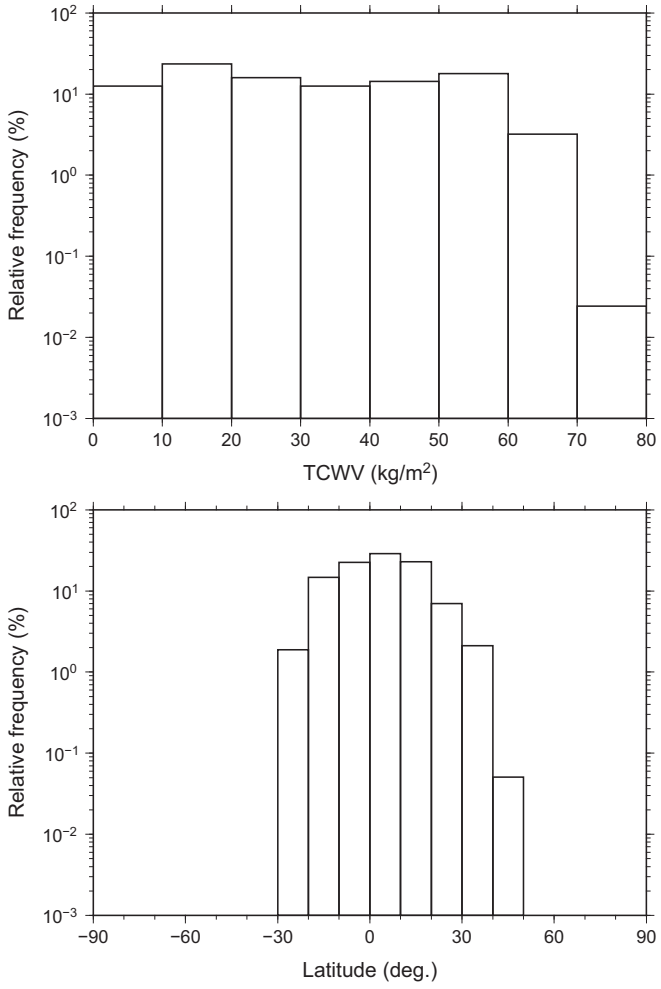

Fig. 11. Frequency of the total column water (TCWV). The top shows relative frequency of TCWV in NWP data; the bottom, the TCWV above 60 kg/m^2 in each latitudinal belt.

method suggest that limited information brought by split-window data

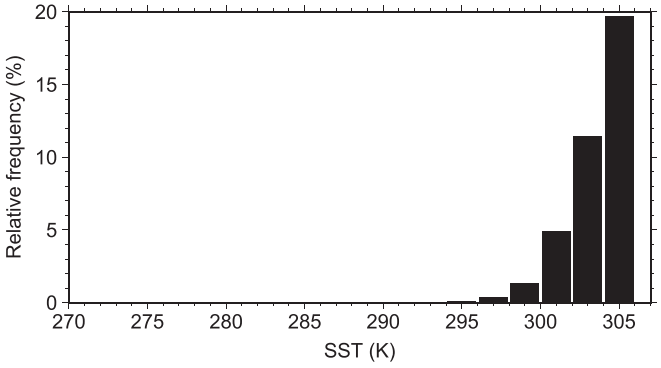

Fig. 12. Frequency of TCWV which above 60 kg/m^2. The histogram shows the rate of TCWV (>60 kg/m^2) at each SST.

is a physical reason for a high negative bias, uncertainty, low sensitivity to SST variation, and low robustness against variations due to WV. N2SSTs showed no high negative bias, likely a benefit of coefficients generated for each region of latitude. The result of N2SST suggests that high negative biases in QSSTs may be improved by expanding the Q-method and using external information. Further improvements to deal

Table 3
N2-scheme and Q-method.

	N2-scheme	Q-method
Satellite data	BT	Radiance
Coefficients	Three latitudinal region×SAZ	BT×BTD×SAZ
SST	Absolute temperature	Radiance (deviation from an anchor point)

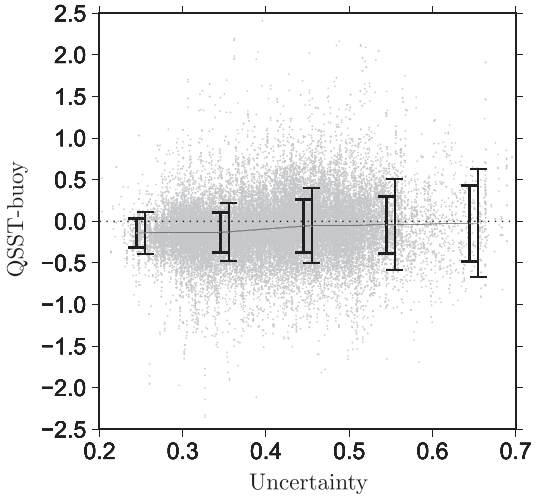

Fig. 13. Determination errors vs. calculated uncertainties. Solid lines and thick error bars denote median and RSTD. Thin error bars and the horizontal axis denote the same uncertainties numerically calculated by taking NEΔT into account.

with high bias are left for the future. Although the impact of aerosols was not serious in this study, robustness against aerosol contributions is an issue with the Q-method, which needs to be improved.

Numerically estimated uncertainties agree with the RSTDs calculated from buoy data. Although they were slightly higher than the RSTDs, the overvalues are not serious, and the estimated uncertainties are meaningful to the NWP and other objective analyses. The authors speculate that this overshoot was caused by nearly saturated WV in NWP data, which is used to calculate uncertainties.

SGLI QSSTs are available at JAXA's websites: the JAXA Globe Portal System (G-Portal),[1] the Satellite Monitoring for Environmental Studies (JASMES)[2] of the JAXA Earth Observation Research Center (EORC), and the Group for High Resolution SST (GHRSST) server.[3]

Declaration of Competing Interest

The authors declare that they have no known competing financial interests or personal relationships that could have appeared to influence the work reported in this paper.

Acknowledgements

Numerical weather prediction (NWP) data and daily SST analysis were generated at the Japan Meteorological Agency (JMA). We used RTTOV 10.2 developed at the Numerical Weather Prediction Satellite Application Facility (NWP SAF) of the European Organisation for the

[1] https://gportal.jaxa.jp/gpr/?lang=en
[2] https://kuroshio.eorc.jaxa.jp/JASMES/index_catalog.html
[3] https://suzaku.eorc.jaxa.jp/GHRSST/index.html

Exploitation of Meteorological Satellites (EUMETSAT). Buoy data were downloaded from the In-situ SST quality monitor (*i*Quam) v2.0 of the National Oceanic and Atmospheric Administration (NOAA). We thank Professor Christopher J Merchant and another anonymous reviewer for providing very insightful and fruitful comments.

Appendix A. GCOM-C and SGLI

The GCOM-C satellite was launched from the Tanegashima Space Center by JAXA on 23 December 2017. GCOM-C is one of two satellites in JAXA's GCOM program, the other being GCOM-W (water), which carries the Advanced Microwave Scanning Radiometer (AMSR) -2. GCOM-C follows up on the Advanced Earth Observing Satellite (ADEOS) -II, which observes geophysical parameters related to the global climate system. GCOM-C flies on a sun-synchronous orbit, which descends at around 10:30 am local time. SGLI is the optical sensor onboard the GCOM-C satellite and is the successor to the GLobal Imager (GLI) onboard the ADEOS-II satellite. SGLI consists of two components, the Visible and Near Infrared Radiometer (VNR) and the Infrared Scanner (IRS). The VNR has 11 non-polarized channels and two polarized channels, and the IRS has four short-wavelength infrared channels and two thermal infrared (or the split-window) channels. The swath width of the VNR is 1150 km. that of the IRS, 1400 km. The spatial resolution can be switched between 250×250 m and 1×1 km. Land and the ocean near shores are scanned with 250×250 m resolution, and the open ocean is scanned with 1×1 km resolution, taking two to three days to cover the whole globe. The resolution is changed following a programmed schedule. The specifications of GCOM-C and SGLI are presented in Tables A.4 and A.5.

Table A.4
GCOM-C specifications.[a]

Item	Specification
Instrument	Second Generation Global Imager (SGLI)
Launch date	23 Dec. 2017
Mission Life	5 years
Power	4250 w (EOL)
Weight	2020 kg
Dimension	Dual solar-paddle design 4.6 m (X) x 16.3 m (Y) x 2.8 m (Z)
Orbit	Sun-synchronous
Altitude	798 km
Inclination	98.6 deg.
Descending local time	10:30±15 min.

[a] https://suzaku.eorc.jaxa.jp/GCOM_C/index.html

Table A.5
SGLI channel specifications.

Ch.**	λ	$\Delta\lambda$	L_{std}, L_{max}		SNR at L_{std}	IFOV
	[nm]	[nm]	[$W/m^2/sr/\mu m$]			[m]
VN1	380	10	60	240–241	624–675	250 / 1000
VN2	412	10	75	305–318	786–826	250 / 1000
VN3	443	10	64	457–467	487–531	250 / 1000
VN4	490	10	53	147–150	858–870	250 / 1000
VN5	530	20	41	361–364	457–522	250 / 1000
VN6	565	20	33	95–96	1027–1064	250 / 1000
VN7	673.5	10	23	69–70	988–1088	250 / 1000
VN8	673.5	20	25	213–217	537–564	250 / 1000
VN9	763	8	40	351–359	1592–1746	1000
VN10	868.5	20	8	37–38	470–510	250 / 1000
VN11	868.5	20	30	305–306	471–511	250 / 1000
P1	670	20	25	293	609	1000
P2	865	20	30	396	646	1000
SW1	1050	20	57	289.2	951.8	1000
SW2	1380	20	8	118.9	347.3	1000
SW3	1640	200	3	50.6	100.5	250 / 1000
SW4	2210	50	1.9	21.7	378.7	1000
Ch.	λ	$\Delta\lambda$	T_{std}, T_{max}		NEΔT at T_{std}	IFOV
	[μm]	[μm]	[K]			[m]
T1	10.8	0.7	300	340	0.08	250 / 500 / 1000
T2	12.0	0.7	300	340	0.13	250 / 500 / 1000

L: signal level, SNR: signal noise ratio, NEΔT: noise equivalent temperature difference, VN, P: non-polarization and polarization channel of VNR. SW, T: short-wavelength-infrared and thermal infrared channel of IRS.

Appendix B. Conversion from I_s to T_s

This appendix presents a conversion method from radiance to brightness temperature by taking the relative sensor response into account. See Appendix D for the notation used in the discussion.

The relation between the monochromatic radiance and the brightness temperature follows the Planck's law:

$$B_\lambda(T) = \frac{2hc^2}{\lambda^5\left(e^{\frac{hc}{\lambda kT}} - 1\right)}. \tag{B.1}$$

On the other hand, the radiance obtained on a spectral channel of the optical sensor is generally given by a channel-specific function:

$$B(T) = \frac{\int_\lambda P(\lambda) B_\lambda(T) d\lambda}{\int_\lambda P(\lambda) d\lambda}. \tag{B.2}$$

Here, $P(\lambda)$ denotes the relative sensor response function (RSR). The RSR gives a weight for each wavelength that is specific to the spectral channel. Hence, the inverse transformation from $B(T)$ to T also needs to consider the effect of the RSR. It is also the same for converting the surface radiance to SST. We introduced an extended inverse of the Planck function:

$$T_s = \phi_1 \cdot B_{\lambda_1}^{-1}(I_s) \tag{B.3}$$

to take the RSR of SGLI into account approximately. Here, the middle dot denotes the function composition. Because I_s is calculated at T1, λ_1 denotes the central wavelength of T1. The ϕ_1:

$$\phi_1(T) = \sum_{k=0}^{n} b_k T^k \tag{B.4}$$

is the regression formula for taking into account the RSR of T1. Coefficients are generated by performing a regression analysis of the temperatures T and $T' = B_{\lambda 1}^{-1} \cdot B_1(T)$. Here, B_1 denotes the channel-specific function for T1. We adopted $n = 2$ as the degree of ϕ_1 for SGLI. Note that residuals of ϕ_1 are negligibly small.

Appendix C. Mathematical background of the Q-method

The mathematical process to derive the Q-method from the radiative transfer equation is discussed here, as well as the uncertainty of the method. Notations used in the discussion are summarized in Appendix D.

C.1. Local linearity

The Q-method is calculated assuming the local linearity defined below.

Let $I = F(\mathbf{x})$ denote the radiative transfer from the sea surface to the top of the atmosphere. Here, I is the radiance at the top of the atmosphere and F denotes the radiative transfer function. The $\mathbf{x}$ is a column vector of parameters that affects radiative transfer. Let us assume that the parameters are not correlated with each other. Note that $\mathbf{x}$ is discussed in the next subsection. The Taylor expansion of F at $\mathbf{x} = \mathbf{x}_0$ is given by

$$I_s = F(\mathbf{x}_0) + \nabla F(\mathbf{x}_0)^T \Delta\mathbf{x} + \cdots \tag{C.1}$$

where $\nabla F(\mathbf{x}_0)$ is a (column) gradient vector at $\mathbf{x} = \mathbf{x}_0$ and $\Delta\mathbf{x}$ is a column vector of the difference between $\mathbf{x}$ and $\mathbf{x}_0$: $\Delta\mathbf{x} = \mathbf{x} - \mathbf{x}_0$.

The original Q-method assumes only

$$I_s = F(\mathbf{x}_0) + \nabla F(\mathbf{x}_0)^T \Delta\mathbf{x} \tag{C.2}$$

for each IR channel. To apply the Q-method to the split-window data of SGLI, we added another assumption:

$$\Delta\mathbf{x}_i = \mathbf{A}\Delta\mathbf{x}_j. \tag{C.3}$$

Here, $\mathbf{A}$ is the matrix. The i and j associated with $\Delta\mathbf{x}$ indicate the IR channel. An added assumption induces a linear model which calculates I_s at IR channel i from $\Delta\mathbf{x}_j$. Because we did not assume (C.3), the original method determines SST by iterative calculations; this is to account for nonlinear relations between IR channels. However, by adding (C.3), the modified method determines SST with a single calculation by a linear model. We consider the extended assumption to be more natural.

C.2. Derivation of the Q-method

The IR radiative transfer under the clear sky condition is formulated by

$$I_\lambda = \left\{ \varepsilon_\lambda B_\lambda(T_s) + (1 - \varepsilon_\lambda) \int_{p_{TOA}}^{p_{srf}} \frac{\partial t_\lambda(p, p_{srf})}{\partial p} B_\lambda(T_p) dp \right\} t_{\lambda(p_{srf}, p_{TOA})} + \int_{p_{srf}}^{p_{TOA}} \frac{\partial t_{\lambda(p, p_{TOA})}}{\partial p} B_\lambda(T_p) dp \tag{C.4}$$

(e.g. Liou, 2002). The $1 - \varepsilon_\lambda$ is the reflectivity of the surface according to Kirchhoff's law (e.g. Liou, 2002, p. 13). Note that the determined reflectivity is an approximation, because Kirchhoff's law may not hold if a strong surface wind makes the sea surface rough. The two integrals denote the integrated intensities of downwelling and upwelling radiations from the atmosphere, respectively. By replacing these integrals with $I_\downarrow$ and $I_\uparrow$, (C.4)

can be rewritten as

$$I = \varepsilon I_s t + (1-\varepsilon) I_\downarrow t + I_\uparrow \tag{C.5}$$

where $B_\lambda(T_s)$ and $t_{\lambda(psrf,pTOA)}$ are simplified to I_s and t; the λ associated with each parameter is omitted.

Then, let $\boldsymbol{x} = (I_s, \tau, I_\uparrow, I_\downarrow, I)^T$ be a column vector of the parameters of (C.5), and $\boldsymbol{x}_0$ be the anchor point vector of $\boldsymbol{x}$ (vectors will be assumed to be column vectors unless otherwise noted). Here, $\tau = -\ ln\,(t)$ is the spectral optical thickness of the atmosphere. We introduced τ because it is determined with a linear function of the radiation path length:

$$\begin{aligned}\tau &= \int_s k_s \rho_s ds \\ &= \overline{k\rho} L\end{aligned} \tag{C.6}$$

where the k and ρ denote the absorption coefficient and density of the atmosphere, respectively (e.g. Liou, 2002, p. 30). L is the total path length from the surface to the top of the atmosphere, and an overline indicates the mean. The total path length is almost a constat at each SZA. The last term is derived by applying the mean value theorem to the second term.

The order of elements is chosen for the convenience of discussion. Note that the result is independent of the order, as will be shown later. Then, consider the formulation of ΔI: the last element of $\Delta\boldsymbol{x} = \boldsymbol{x} - \boldsymbol{x}_0$. However, this is not simple because of mutual dependence between the elements. To avoid complications due to the mutual dependence, we orthogonalized $\Delta\boldsymbol{x}$ by performing Gram-Schmidt (GS) orthogonalization. The GS process orthogonalizes $\Delta\boldsymbol{x}$ by extracting the orthogonal components from the elements. Appendix C.5 discusses the details of the GS. Note that GS is robust against linearity or multicollinearity of the data. GS is performed on $\Delta\boldsymbol{x}$ calculated by using $\boldsymbol{x}$ gathered at each bin (Fig. 1). Here, $\boldsymbol{x}$ is generated by using RTM and NWP data, then, $\boldsymbol{x}_0$ is determined with the following two-step procedure:

1. Each element of $\boldsymbol{x}_0$ is determined by the ensemble average of $\boldsymbol{x}$,
2. Then I_0 is determined from other determined elements by (C.5).

Let $\Delta\mathbf{x} = (\Delta I_s, r_\tau, r_\uparrow, r_\downarrow, r)^T$ be the vector of the orthogonal component determined by performing GS on $\Delta\boldsymbol{x}$. Here, r_τ denotes the orthogonal component of $\Delta\tau$; the same applies to the others. Note that ΔI_s is transformed onto $\Delta\mathbf{x}$ without any change. The coordinate transformation matrix $\mathbf{P}_{\boldsymbol{x}}$, such that

$$\Delta\boldsymbol{x} = \mathbf{P}_{\boldsymbol{x}} \Delta\mathbf{x}, \tag{C.7}$$

is also generated through the GS process. $\mathbf{P}_{\boldsymbol{x}}$ is a lower triangular matrix with non-zero diagonal elements and is invertible. Although $\mathbf{P}_{\boldsymbol{x}}$ depends on the order of the elements of $\boldsymbol{x}$, the results derived from different $\mathbf{P}_{\boldsymbol{x}}$ are equivalent because of the invertibility of $\mathbf{P}_{\boldsymbol{x}}$. Focusing on ΔI, the last element of $\Delta\boldsymbol{x}$, we have

$$\Delta I = a_1 \Delta I_s + a_2 r_\tau + a_3 r_\uparrow + a_4 r_\downarrow + r \tag{C.8}$$

from (C.7). Here, $(a_1, \cdots, a_4, 1)$ is given by the 5^{th}-row vector of $\mathbf{P}_{\boldsymbol{x}}$. Note that there may be fewer than five terms on the right side of (C.8) because of the exclusion of linearly dependent elements through the GS processes.

In SST determination, we have (C.8) for each IR channel. Let n be the total number of the IR channels. Then, (C.3), the extended assumption of local linearity, allows us the linear conversion of $\Delta\mathbf{x}$ between the IR channels, (i.e., $\Delta\mathbf{x}_{\lambda_j} = \mathbf{A}_{(ij)} \Delta\mathbf{x}_{\lambda_i}$ for all i, j of the IR channels). Here, $\mathbf{A}_{(ij)}$ is the matrix of coefficients. Hence, (C.8) for each IR channel can be assembled in vector form:

$$\Delta\mathbf{I} = \mathbf{A}\Delta\mathbf{x}, \tag{C.9}$$

where $\Delta\mathbf{I}$ is the n-vector of ΔI for each IR channel, $\mathbf{A}$ is an m×n-matrix, and $\Delta\mathbf{x}$ is the deviation vector for the first IR channel. Here, m≤5 is the total number of elements of $\Delta\mathbf{x}$. Then, by letting $\mathbf{A}^+$ be the pseudo-inverse of $\mathbf{A}$, we have

$$\Delta\mathbf{x} = \mathbf{A}^+ \Delta\mathbf{I} \tag{C.10}$$

by multiplying both sides of (C.9) by $\mathbf{A}^+$ from the left. $\mathbf{A}^+$ is also referred to as the Moore-Penrose inverse (e.g. Barata and Hussein, 2012). If $\mathbf{A}^T\mathbf{A}$ is invertible, $\mathbf{A}^+$ is given by

$$\mathbf{A}^+ = \left(\mathbf{A}^T\mathbf{A}\right)^{-1}\mathbf{A}^T. \tag{C.11}$$

Here, the invertibility of $\mathbf{A}^T\mathbf{A}$ holds if row vectors of $\mathbf{A}$ are linearly independent of each other. Linear independence of the row vectors could be claimed if the combination of IR channels was suitable for SST determination. Noting that ΔI_s is the first element of $\Delta\mathbf{x}$, it is apparent that the first row vector of $\mathbf{A}^+$, and $\Delta\mathbf{I}$ gives the second term on the right side of (1). Meanwhile, the anchor point gives the first term I_{s_0}. Hence, we finally have (1). Note that $\mathbf{A}$ and $\mathbf{A}^+$ are not commutative in general. Hence, the transformation from (C.9) to (C.10) is not invertible, which suggests the calculation is an approximation.

Matrix $\mathbf{A}$ is determined by performing a regression analysis on $\Delta\mathbf{I}$ and $\Delta\mathbf{x}$. It is also possible to calculate $\mathbf{A}^+$ directly with a regression analysis. In the latter case, $\mathbf{A}^+$ is given by

$$\mathbf{A}^+ = \left(\mathbf{S}_x^{-1}\mathbf{S}_{xy}\right)^T \tag{C.12}$$

where $\mathbf{S}_x$ is the variance-covariance matrix (simply the covariance matrix, hereafter) of $\Delta\mathbf{I}$, and $\mathbf{S}_{xy}$ denotes the covariance matrix of $\Delta\mathbf{I}$ and $\Delta\mathbf{x}$. Here, $\mathbf{S}_x$

and $\mathbf{S}_{xy}$ are determined by $\langle \Delta\mathbf{I}\Delta\mathbf{I}^T \rangle$ and $\langle \Delta\mathbf{I}\Delta\mathbf{x}^T \rangle$, respectively. It is easily confirmed that the first vector of $\mathbf{S}_{xy}$ is given by $\langle \Delta I_s \Delta\mathbf{I} \rangle$. Therefore, the coefficient vector $\mathbf{a}$ in (1) is determined only from ΔI_s and $\Delta\mathbf{I}$, and is not affected by other orthogonal components. Let $\mathbf{S}_e$ be the covariance matrix of the sensor-specific noise. Then, $\mathbf{A}^+$ is calculated by taking the sensor noise into account by

$$\mathbf{A}^+ = \mathbf{S}_{xy}^T \left(\mathbf{S}_x^{-1} + \mathbf{S}_e \right)^T. \tag{C.13}$$

Note that the discussion above applies to other Δ values, which suggests that other parameters can be determined similarly.

C.3. Uncertainty

Uncertainties originating from the Q-method are given by the residuals with the regression model $\mathbf{A}^+$. Here, a residual is a deviation of $\mathbf{A}^+\Delta\mathbf{I}$ from $\Delta\mathbf{x}$. Let $\mathbf{S}_r$ be the covariance matrix of the residuals, then, the method-generated uncertainty is given by the diagonal elements of $\mathbf{S}_r$:

$$\mathbf{S}_r = \left\langle (\mathbf{A}^+\Delta\mathbf{I} - \Delta\mathbf{x})(\mathbf{A}^+\Delta\mathbf{I} - \Delta\mathbf{x})^T \right\rangle \tag{C.14}$$

On the other hand, discrepancies between determined SSTs and the true values originating from sensor noise can be calculated by $\mathbf{A}^+\mathbf{e}$ where $\mathbf{e}$ denotes the vector of the sensor noise. Let $\mathbf{S}_n$ be the covariance matrix of $\mathbf{A}^+\mathbf{e}$. Then, $\mathbf{S}_n$ is derived by

$$\begin{aligned} \mathbf{S}_n &= \left\langle (\mathbf{A}^+\mathbf{e})(\mathbf{A}^+\mathbf{e})^T \right\rangle \\ &= \mathbf{A}^+\mathbf{S}_e(\mathbf{A}^+)^T, \end{aligned} \tag{C.15}$$

where $\mathbf{S}_e$ denotes the covariance matrix of $\mathbf{e}$, i.e., $\mathbf{S}_e = \langle \mathbf{e}\mathbf{e}^T \rangle$. Finally, the total uncertainties in determined SSTs are given by

$$\mathbf{S}_r + \mathbf{S}_n. \tag{C.16}$$

Note that (C.16) does not include the uncertainties originating from the anchor points and coefficients which are generated by using RTM and NWP data. Degradations caused by cloud masking errors are also not included.

C.4. Validity of the extension of local linearity

The extended assumption of local linearity, (C.3) is directly connected to the derivation of (C.9). Hence, the degradation originating from the assumption is evaluated by examining the variance of $\Delta\mathbf{I} - \mathbf{A}\Delta\mathbf{x}$. Let $\mathbf{S}_a$ be the covariance matrix of $\Delta\mathbf{I} - \mathbf{A}\Delta\mathbf{x}$. Then, $\mathbf{S}_a$ is calculated by

$$\mathbf{S}_a = \left\langle (\Delta\mathbf{I} - \mathbf{A}\Delta\mathbf{x})(\Delta\mathbf{I} - \mathbf{A}\Delta\mathbf{x})^T \right\rangle \tag{C.17}$$

Regarding the SGLI, the variance has been estimated to be 0.022–0.026 K for T2, which is given by the second diagonal element of $\mathbf{S}_a$. Also, the nominal value of the noise equivalent temperature difference (NEΔT) is 0.13 K for T2 (Table A.5). Hence, the estimated degradation is 0.0026 $\approx \sqrt{0.13^2 + 0.026^2} - 0.13$ (K) at the maximum of T2. Therefore, the impact of the assumption is considered to be negligible. Note that T1 is not affected by the extension.

C.5. Gram-Schmidt process

The Gram-Schmidt process (GS) is a method to orthogonalize the vectors in the Euclidean space. However, it is also possible to orthogonalize two or more correlated variables similarly, also called GS here.

Let $\mathbf{u} = (u_i)$ be a vector and U be a set of $\mathbf{u}$, and let $\mathbf{v} = (v_i)$ and V be the vector and its set generated by performing GS on $\mathbf{u} \in U$. Here, let us assume that $<\mathbf{u}>_{\mathbf{u}\in U} = \mathbf{0}$. Then, each $\mathbf{v} \in V$ is derived by a GS iteration as seen here

$$\begin{cases} v_1 = u_1 \\ v_i = u_i - \sum_{j=1}^{i-1} \dfrac{< u_i v_j >}{< v_j^2 >} v_j \quad \text{for } i > 1. \end{cases} \tag{C.18}$$

Here, ensemble averages are calculated using $\mathbf{u} \in U$ and $\mathbf{v} \in V$. It is not difficult to show that $\mathbf{v}$ satisfies $\langle v_i v_j \rangle_{\mathbf{v}\in V} = 0$ for all pairs of i, j ($i \neq$j). For example, $<v_1 v_2> = 0$ is shown as:

$$\begin{aligned} &\langle v_1 v_2 \rangle = \langle u_1 v_2 \rangle \\ &= \left\langle u_1 \left(u_2 - \frac{\langle u_1 u_2 \rangle}{\langle u_1^2 \rangle} u_1 \right) \right\rangle \\ &= \langle u_1 u_2 \rangle - \frac{\langle u_1 u_2 \rangle}{\langle u_1^2 \rangle} \langle u_1^2 \rangle \\ &= 0, \end{aligned} \tag{C.19}$$

and the same for the others. Let $\mathbf{P} = (p_{ij})$ be the coordinate transformation matrix from V to U. Then, $\mathbf{P}$ is given by

$$\begin{cases} p_{ij} = \dfrac{\langle u_i v_j \rangle}{\langle v_j^2 \rangle} \\ p_{ij} = 0 \qquad \text{if } i < j. \end{cases} \tag{C.20}$$

GS will fail at the $(i+1)$-th process if u_i linearly depends on some u_j $(j<i)$, (i.e., if u_i is written as $u_i = \sum_{j<i} a_j u_j$). However, the failure can be avoided by excluding u_i. Linear dependence can be determined by examining v_i for its variance because $\langle v_i^2 \rangle = 0$ if u_i depends on some u_j. Note that this exclusion does not harm the result because the excluded u_i can be retrieved using the remaining orthogonalized parameters. In computer calculations, computational instability can occur with an extremely small variance of v_i. To avoid this, the variance of v_i should be examined through the process.

Lastly, here is an important point. This discussion has assumed that $\langle \mathbf{u} \rangle = \mathbf{0}$. However, for the ΔI of the Q-method, its average is not zero because of the nonlinearity of the radiative transfer Eq. (C.4). To avoid unexpected results, we adjusted each ΔI by $\Delta I - \langle \Delta I \rangle$ so that ΔI has an average of zero. However, this adjustment is performed only for GS, otherwise the result will be incorrect such that $\Delta I \neq 0$ at $\Delta \mathbf{x} = 0$ (Fig. C.14).

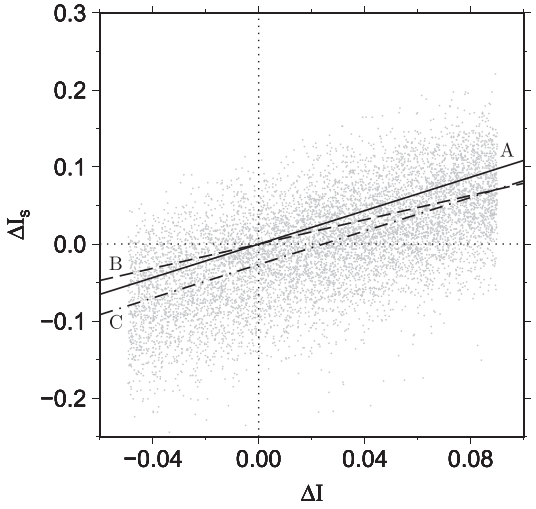

Fig. C.14. First-order approximations of ΔI_s by ΔI. Gray dots are the data to be fitted. A is an approximation line calculated from offset-adjusted ΔI ($\Delta I - \langle \Delta I \rangle$). B was calculated by performing a regression analysis, and C was derived by adding the offset of $\langle \Delta I \rangle$ to ΔI of A to restore the original ΔI. A was adopted for the Q-method. B generates bias different at the ends of the range of ΔI, although it makes the variation of residuals minimum. C generates negative bias as clear from the y-coordinate of the y-intercept.

Appendix D. Notation

This appendix summarizes the notation used in the discussions.

Notation	Description
B	Planck function
c	The velocity of light
h	Planck's constant
I	Radiance
I_s	Sea surface radiance
$I_\uparrow$	Total atmospheric upwelling radiance
$I_\downarrow$	Total atmospheric downwelling radiance
K	Boltzmann's constant
ln	Natural logarithm
p	Atmospheric pressure
p_{srf}	Atmospheric pressure at the Earth surface
p_{TOA}	Atmospheric pressure at the top of the atmosphere
sec	The secant function
T	Absolute temperature
T_s	Sea surface temperature (SST)
t	Transmittance
ε	Sea surface emissivity
θ	Zenith angle
λ	Wave length
σ^2	Variance
τ	Spectral optical thickness
x_0, Δx	An anchor point and the deviation from the anchor point $(x - x_0)$
$\boldsymbol{x}$	Vector on a oblique coordinate system
$\mathbf{A}$, $\mathbf{x}$	Matrix, vector on the Cartesian coordinates
$\mathbf{A}^T$, $\mathbf{x}^T$, $\boldsymbol{x}^T$	Transpose of matrix, vector
$\mathbf{A}^{-1}$, f^{-1}	Inverse of matrix, function
$\mathbf{A}^+$	Pseudo-inverse of matrix
$\langle\ \rangle$	Ensemble mean
$\cdot$	Function composition

References

Anding, D., Kauth, R., 1970. Estimation of sea surface temperature from space. Remote Sens. Environ. 1, 217–220.

Barata, J.C.A., Hussein, M.S., 2012. The Moore–Penrose pseudoinverse: A tutorial review of the theory. Braz. J. Phys. 42, 146–165.

Beggs, H., Morgan, N., Sisson, J., 2017. IMOS ship SST for satellite SST validation. In: Proceedings of the GHRSST XVIII Science Team Meeting, Qingdao, China, pp. 5–9.

Casey, K.S., Brandon, T.B., Cornillon, P., Evans, R., 2010. The past, present, and future of the AVHRR pathfinder SST program. In: Barale, V., Gower, J., Alberotanza, L. (Eds.), Oceanography from Space: Revisited. Springer Netherlands, Dordrecht, pp. 273–287.

Donlon, C., Robinson, I.S., Wimmer, W., Fisher, G., Reynolds, M., Edwards, R., Nightingale, T.J., 2008. An infrared sea surface temperature autonomous radiometer (ISAR) for deployment aboard volunteer observing ships (VOS). J. Atmos. Ocean. Technol. 25, 93–113.

Donlon, C.J., Nightingale, T.J., Sheasby, T., Turner, J., Robinson, I.S., Emergy, W.J., 1999. Implications of the oceanic thermal skin temperature deviation at high wind speed. Geophys. Res. Lett. 26, 2505–2508.

Embury, O., Merchant, C.J., 2012. A reprocessing for climate of sea surface temperature from the along-track scanning radiometers: a new retrieval scheme. Remote Sens. Environ. 116, 47–61 (Advanced Along Track Scanning Radiometer(AATSR) Special Issue).

Embury, O., Merchant, C.J., Corlett, G.K., 2012a. A reprocessing for climate of sea surface temperature from the along-track scanning radiometers: initial validation, accounting for skin and diurnal variability effects. Remote Sens. Environ. 116, 62–78 (Advanced Along Track Scanning Radiometer(AATSR) Special Issue).

Embury, O., Merchant, C.J., Filipiak, M.J., 2012b. A reprocessing for climate of sea surface temperature from the along-track scanning radiometers: basis in radiative transfer. Remote Sens. Environ. 116, 32–46 (Advanced Along Track Scanning Radiometer(AATSR) Special Issue).

Fairall, C., Bradley, E.F., Godfrey, J., Wick, G., Edson, J.B., Young, G., 1996. Cool-skin and warm-layer effects on sea surface temperature. J. Geophys. Res. 101, 1295–1308.

Foltz, G.R., McPhaden, M.J., 2008. Impact of Saharan dust on tropical North Atlantic SST. J. Clim. 21, 5048–5060.

Gentemann, C.L., Donlon, C.J., Stuart-Menteth, A., Wentz, F.J., 2003. Diurnal signals in satellite sea surface temperature measurements. Geophys. Res. Lett. 30.

Huber, P.H., Ronchetti, E.M., 2009. Robust Statistics. John Wiley & Sons, Second Edition.

Ignatov, A., Zhou, X., Petrenko, B., Liang, X., Kihai, Y., Dash, P., Stroup, J., Sapper, J., DiGiacomo, P., 2016. AVHRR GAC SST reanalysis version 1 (RAN1). Remote Sens. 8, 315.

Imaoka, K., Kachi, M., Fujii, H., Murakami, H., Hori, M., Ono, A., Igarashi, T., Nakagawa, K., Oki, T., Honda, Y., Shimoda, H., 2010. Global change observation mission (GCOM) for monitoring carbon, water cycles, and climate change. Proc. IEEE 98, 717–734.

Inoue, T., 1987. A cloud type classification with NOAA 7 split-window measurements. J. Geophys. Res.-Atmos. 92, 3991–4000.

Kilpatrick, K., Podestá, G., Walsh, S., Williams, E., Halliwell, V., Szczodrak, M., Brown, O., Minnett, P., Evans, R., 2015. A decade of sea surface temperature from MODIS. Remote Sens. Environ. 165, 27–41.

Kilpatrick, K.A., Podestá, G.P., Evans, R., 2001. Overview of the NOAA/NASA advanced very high resolution radiometer pathfinder algorithm for sea surface temperature and associated matchup database. J. Geophys. Res. Oceans 106, 9179–9197.

Koner, P.K., Harris, A., Maturi, E., 2015. A physical deterministic inverse method for operational satellite remote sensing: an application for sea surfacetemperature retrievals. IEEE Trans. Geosci. Remote Sens. 53, 5872–5888.

Kurihara, Y., Murakami, H., Kachi, M., 2016. Sea surface temperature from the new Japanese geostationary meteorological Himawari-8 satellite. Geophys. Res. Lett. 43 (3), 1234–1240 ((pp. n/a–n/a). 2015GL067159).

Liou, K.-N., 2002. An Introduction to Atmospheric Radiation, vol. 84. Academic press.

Masuda, K., Takashima, T., Takayama, Y., 1988. Emissivity of pure and sea waters for the model sea surface in the infrared window regions. Remote Sens. Environ. 24, 313–329.

McClain, E., Pichel, W., Walton, C., Ahmad, Z., Sutton, J., 1983. Multi-channel improvements to satellite-derived global sea surface temperatures. Adv. Space Res. 2, 43–47.

McClain, E.P., Pichel, W.G., Walton, C.C., 1985. Comparative performance of AVHRR-based multichannel sea surface temperatures. J. Geophys. Res. 90, 11587.

McMillin, L.M., 1975. Estimation of sea surface temperatures from two infrared window measurements with different absorption. J. Geophys. Res. 80, 5113–5117.

Merchant, C., Le Borgne, P., Roquet, H., Marsouin, A., 2009a. Sea surface temperature from a geostationary satellite by optimal estimation. Remote Sens. Environ. 113, 445–457.

Merchant, C.J., Le Borgne, P., Marsouin, A., Roquet, H., 2008. Optimal estimation of sea surface temperature from split-window observations. Remote Sens. Environ. 112, 2469–2484.

Merchant, C.J., Harris, A.R., Roquet, H., Le Borgne, P., 2009b. Retrieval characteristics of non-linear sea surface temperature from the advanced very high resolution radiometer. Geophys. Res. Lett. 36 (n/a–n/a. L17604).

Merchant, C.J., Embury, O., Bulgin, C.E., Block, T., Corlett, G.K., Fiedler, E., Good, S.A., Mittaz, J., Rayner, N.A., Berry, D., Eastwood, S., Taylor, M., Tsushima, Y., Waterfall, A., Wilson, R., Donlon, C., 2019. Satellite-based time-series of sea-surface temperature since 1981 for climate applications. Sci. Data 6, 223.

Minnett, P., Alvera-Azcárate, A., Chin, T., Corlett, G., Gentemann, C., Karagali, I., Li, X., Marsouin, A., Marullo, S., Maturi, E., Santoleri, R., Picart, S.S., Steele, M., Vazquez-Cuervo, J., 2019. Half a century of satellite remote sensing of sea-surface temperature. Remote Sens. Environ. 233, 111366.

Minnett, P.J., Knuteson, R., Best, F., Osborne, B., Hanafin, J., Brown, O., 2001. The marine-atmospheric emitted radiance interferometer: a high-accuracy, seagoing infrared spectroradiometer. J. Atmos. Ocean. Technol. 18, 994–1013.

Nalli, N.R., Smith, W.L., 1998. Improved remote sensing of sea surface skin temperature using a physical retrieval method. J. Geophys. Res. Oceans 103, 10527–10542.

O'Carroll, A.G., Armstrong, E.M., Beggs, H.M., Bouali, M., Casey, K.S., Corlett, G.K., Dash, P., Donlon, C.J., Gentemann, C.L., Høyer, J.L., Ignatov, A., Kabobah, K., Kachi, M., Kurihara, Y., Karagali, I., Maturi, E., Merchant, C.J., Marullo, S., Minnett, P.J., Pennybacker, M., Ramakrishnan, B., Ramsankaran, R., Santoleri, R., Sunder, S., Saux Picart, S., Vázquez-Cuervo, J., Wimmer, W., 2019. Observational needs of sea surface temperature. Front. Mar. Sci. 6, 420.

Pavolonis, M.J., 2010. Advances in extracting cloud composition information from spaceborne infrared radiances—A robust alternative to brightness temperatures. Part I: Theory. J. Appl. Meteorol. Climatol. 49, 1992–2012.

Petrenko, B., Ignatov, A., Kihai, Y., Stroup, J., Dash, P., 2014. Evaluation and selection of SST regression algorithms for JPSS VIIRS. J. Geophys. Res.-Atmos. 119, 4580–4599 (2013JD020637).

Prabhakara, C., Dalu, G., Kunde, V.G., 1974. Estimation of sea surface temperature from remote sensing in the 11- to 13-μm window region. J. Geophys. Res. 79, 5039–5044.

Reynolds, R.W., 1993. Impact of mount Pinatubo aerosols on Satellite-Derived Sea surface temperatures. J. Clim. 6, 768–774.

Roberts, R.E., Selby, J.E.A., Biberman, L.M., 1976. Infrared continuum absorption by atmospheric water vapor in the 8–12-μm window. Appl. Opt. 15, 2085–2090.

Saunders, R., Hocking, J., Rayer, P., Matricardi, M., Geer, A., Bormann, N., Brunel, P., Karbou, F., Aires, F., 2012. RTTOV-10 science and validation report. In: EUMETSAT, NWPSAT-MO-TV-023, p. 31.

Smith, W.L., Woolf, H.M., Revercomb, H.E., 1991. Linear simultaneous solution for temperature and absorbing constituent profiles from radiance spectra. Appl. Opt. 30, 1117–1123.

Walton, C.C., Pichel, W.G., Sapper, J.F., May, D.A., 1998. The development and operational application of nonlinear algorithms for the measurement of sea surface temperatures with the NOAA polar-orbiting environmental satellites. J. Geophys. Res. 103, 27999.

Watts, P.D., Allen, M.R., Nightingale, T.J., 1996. Wind speed effects on sea surface emission and reflection for the along track scanning radiometer. J. Atmos. Ocean. Technol. 13, 126–141.

Xu, F., Ignatov, A., 2014. In situ SST quality monitor (iQuam). J. Atmos. Ocean. Technol. 31, 164–180.

Yang, M., Guan, L., Beggs, H., Morgan, N., Kurihara, Y., Kachi, M., 2020. Comparison of Himawari-8 AHI SST with shipboard skin SST measurements in the Australian region. Remote Sens. 12.

Yoshida, M., Yumimoto, K., Nagao, T.M., Tanaka, T., Kikuchi, M., Murakami, H., 2020. Retrieval of aerosol combined with assimilated forecast. Atmos. Chem. Phys. Discuss. 2020, 1–19.

Závody, A.M., Mutlow, C.T., Llewellyn-Jones, D.T., 1995. A radiative transfer model for sea surface temperature retrieval for the along-track scanning radiometer. J. Geophys. Res. Oceans 100, 937–952.